catalysts

MDPI

Review

Dimension Engineering in Noble-Metal-Based Nanocatalysts

Bei Liu [1,†], Haosen Yang [2,†], Pengfei Hu [1,2,*], Guang-Sheng Wang [2], Yongqiang Guo [2] and Hewei Zhao [2,*]

[1] Research Institute of Aero-Engine, Beihang University, Beijing 102206, China; lb010928@buaa.edu.cn
[2] School of Chemistry, Key Laboratory of Bio-Inspired Smart Interfacial Science and Technology, Beijing Advanced Innovation Center for Biomedical Engineering, Beihang University, Beijing 100191, China; yanghaosen@buaa.edu.cn (H.Y.); wanggsh@buaa.edu.cn (G.-S.W.); gyqnpu@163.com (Y.G.)
* Correspondence: hupengfei@buaa.edu.cn (P.H.); zhaohewei@buaa.edu.cn (H.Z.)
† These authors contributed equally to this work.

Abstract: Catalysts play a pivotal role in modern industries, such as energy, pharmaceuticals, and petrochemicals, serving as cornerstone of high-tech production. Noble metals, such as gold, silver, and platinum group elements, possess the superb catalytic characteristics of high-temperature oxidation resistance, corrosion resistance, stable electrochemical performance, high catalytic activity, and so on. These characteristics offer excellent prospects for applications in catalysis. In this review, we summarize innovative approaches to regulating the size and morphology of nano-noble metal catalysts with different dimensions. We also showcase typical prominent examples of their applications in exhaust gas purification, battery manufacturing, water splitting, and selective hydrogenation. Finally, perspectives are discussed in terms of future research opportunities in the realm of noble metal nanocatalysts.

Keywords: catalysts; nanomaterials; noble metals; dimension engineering

Citation: Liu, B.; Yang, H.; Hu, P.; Wang, G.-S.; Guo, Y.; Zhao, H. Dimension Engineering in Noble-Metal-Based Nanocatalysts. *Catalysts* **2024**, *14*, 9. https://doi.org/10.3390/catal14010009

Academic Editors: Menggang Li, Shuo Geng and Manyi Gao

Received: 15 November 2023
Revised: 13 December 2023
Accepted: 18 December 2023
Published: 20 December 2023

1. Introduction

Catalysts play a vital role in industrial production by altering the reaction rate without affecting the total standard Gibbs free energy of the reaction. The use of microorganisms and biological enzymes as catalysts to brew wine and pickles represents one of the earliest and simplest applications of this concept. The earliest industrial catalysis can be traced back to the lead chamber method for sulfuric acid. Since the onset of the industrial revolution, catalytic technology has developed rapidly and plays a crucial role in contemporary industrial production and scientific research.

The noble metals encompass eight metal elements: gold, silver, platinum, ruthenium, rhodium, palladium, osmium, and iridium. Owing to their chemical stability, corrosion resistance, and unique electronic structure, they are considered the most suitable choice for synthesizing high-quality and efficient catalysts. In recent years, a growing number of researchers have directed their attention toward noble metal nanomaterials (NMNs). With the continuous innovation in nanostructures and the ongoing progress in synthesis technology, the specific surface area of NMNs can be further increased, leading to a higher density of active sites. We can even realize the full utilization of noble metal atoms, which significantly enhances the catalytic activity of precious metal nanocatalysts. The selectivity, durability, and anti-toxicity of the catalysts can also be enhanced by modifying the crystal size, morphology, grain boundaries, and crystal structure to cater to the demands of intricate environments. Therefore, it is crucial to have precise size control of noble metal nanocatalysts.

From the perspective of structure, NMNs include zero-dimensional (0D) NMNs, one-dimensional (1D) NMNs, two-dimensional (2D) NMNs, and three-dimensional (3D) NMNs. These variously structured NMNs exhibit distinctive and exceptional physical and chemical properties. However, synthesizing efficient and cost-effective NMNs necessitates identifying appropriate structures and preparation methods in a challenging but essential pursuit.

This review offers an overview of the diverse structures of NMNs, explores the structure–activity relationship, and discusses new methods for regulating size and morphology across different dimensions, supported by illustrative examples. Then, the applications of NMNs in exhaust gas purification and battery manufacturing are introduced. Finally, the research offers a forward-looking prospective on the research prospects regarding NMNs.

2. NMNs with Different Dimensions

2.1. 0D NMNs

We can define 0D nanostructures as materials at the nanoscale (approximately 100 nm), with 3D spatial dimensions, including quantum dots, nanoclusters, and nanoparticles (NPs). A nanocluster is a molecular-like structure formed by a certain number of atoms, molecules, or ions, with a size that does not generally exceed 10 nm.

Due to the unique structure of 0D nanomaterials, they usually have significant quantum size effects, small size effects, surface effects, and macroscopic quantum tunneling effects. Additionally, their energy level structure and electronic structure are fundamentally different from other multi-dimensional structures, often showing different activity and selectivity from multidimensional nanomaterials.

In essence, the strategies for synthesizing NMNs are mainly divided into two types. The top-down strategy involves the use of complex macroscopic materials and costly technologies to continuously reduce the size of bulk materials or incorporate nanoscale features, including lithography, electron beam lithography, immersion lithography, molecular beam epitaxy, etc. On the other hand, the bottom-up strategy involves aggregating and nucleating molecular or atomic-scale primitives, which then grow to form nanomaterials, including water/solvent chemical synthesis, chemical vapor deposition (CVD), etc. The bottom-up strategy has attracted more attention, and a large number of NMNs are synthesized using this strategy, since they are usually cheaper and easily controlled during the synthesis process through the manipulation of many experimental parameters, including the temperature, precursor properties, stabilizers, solvents, reducing agents, their molar ratio, concentration, etc., and there is the ability to reach an industrial scale. It is worth noting that, unlike 2D NMNs, NMNs in other dimensions rarely use the top-down synthesis strategy.

The main synthesis methods of 0D NMNs include the solvothermal/hydrothermal method, wet chemical synthesis method, dealloying method, template-assisted method, and so on. Li et al. report a Pt-Ru nanocluster prepared via the one-pot hydrothermal method [1]. As seen in Figure 1a, in the synthesis process, Pt^{2+} is firstly reduced and grows into sub-particles as heterogeneous nuclear sites, and then Pt-Ru bimetallic nanoclusters are formed with Ru deposited on the surface of the Pt sub-particles. The Pt-Ru nanoclusters exhibit a porous cluster structure formed through the aggregation, attachment, and assembly of sub-particles, and obvious gaps and micropores could be observed between these Pt sub-particles. As is shown in Figure 1b, Cao et al. synthesize Ru nanodots within interlayers of TiO_2 by etching the $K_2Ti_2O_5$ precursor using salicylic acid, followed by Ru^{3+} exchange and annealing to construct a TiO_2 | Ru | TiO_2 sandwich structure [2]. In this sandwich structure, most Ru nanodots exhibit a diameter of 1.6 nm, and they are in close contact with the anatase TiO_2 layer, which promotes electron transfer and limits the aggregation of Ru nanodots. Liang et al. synthesize 0D Ag NPs via a selective aqueous corrosion method [3], which is schematically illustrated in Figure 1c. Through the selective aqueous corrosion process of the Mg_xAg alloy, black Ag NPs are embedded in the gray matrix of $Mg(OH)_2$ and alloys. Then, 0D Ag NPs with an average diameter of 22 ± 4 nm can be obtained after acid washing. In the selective aqueous corrosion process, the pH value of the aqueous solution promotes the dealloying process and growth of Ag NPs. Li et al. use an albumin template to synthesize PtS(II) nanodots (NDs) with a controllable size [4]. Pt^{2+} is induced via electrostatic interaction with albumin, followed by nucleation and growth in albumin nanocages. It can be seen from Figure 1d that the prepared PtS NDs exhibit a diameter of

4.5 ± 0.4 nm, a spherical morphology, and good dispersibility, which indicates that the growth of PtS NDs is precisely controlled in albumin nanocages.

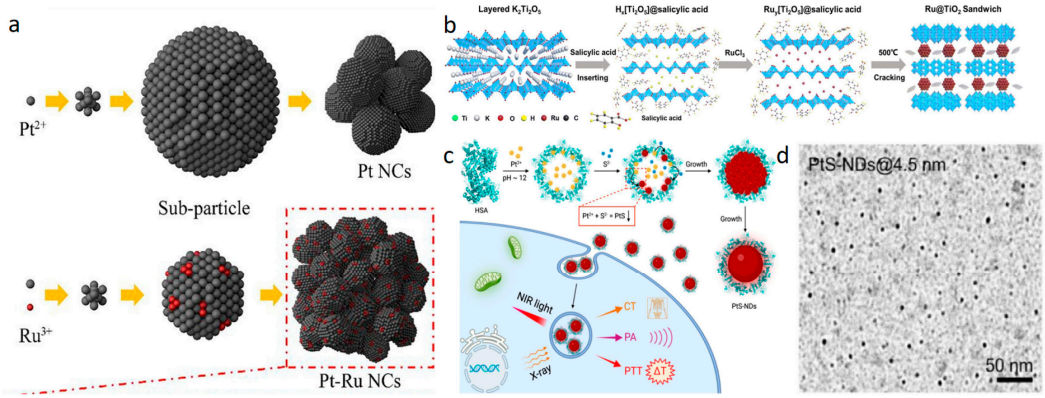

Figure 1. Schematic illustration of the synthesis of (**a**) Pt nanoclusters and Pt-Ru nanoclusters. Reprinted from [1] with Permission from ELSEVIER, 2023, (**b**) Ru@TiO_2 sandwich. Reprinted from [2] with Permission from RSC, 2023, and (**c**) PtS NDs. Reprinted from [3] with Permission from RSC, 2019; (**d**) TEM (transmission electron microscope) image of PtS NDs. Reprinted from [4] with Permission from ELSEVIER, 2023.

Noble-metal single-atom catalysis (NMSAC) has become a frontier of catalysis due to its extremely high atomic utilization and corresponding high catalytic activity. NMSAC refers to noble metals atomically dispersed on solid supports. Zhang's group fabricated Pt_1/FeO_x SAC by anchoring single Pt atoms on the surface of FeO nanocrystals [5]. The Pt_1/FeO_x SAC exhibited excellent stability and activity for both CO oxidation and the preferential oxidation of CO in H_2. In addition, NMSAC has a higher catalytic performance than noble metal nanoparticle catalysts in some catalytic systems. Zhu et al. report that the strong adsorption of CO_2 on Rh single atoms and the corresponding low activation energy lead to the conversion rate of CO_2 being two orders of magnitude higher than that of Rh NPs [6]. In pursuit of 100% atomic utilization, the stability of NMSAC is pivotal. Mochizuki et al. use defective NiO as a stabilizer for Au SAC [7]. DFT calculations show that the formation of Au single atoms is more favorable on a defective NiO surface with Ni vacancy sites than on a smooth NiO surface. Meanwhile, using CO oxidation as a stability test, no significant decrease in CO conversion has been observed even after 120 h. This fully demonstrates the importance of cationic defect sites for the stability of Au single-atoms.

Double-atom catalysts (DACs), also known as dual-atom catalysts, perfectly inherit the advantages of SACs' 100% active atom utilization. Meanwhile, there are internuclear electron interactions between dinuclear sites, and this results in dinuclear co-adsorption and catalytic cooperative interactions, which can overcome the limitation of the intermediate adsorption correlation of mononuclear sites, greatly improving the catalytic activity and selectivity of DACs. A typical example is Pt_2 DACs for the selective hydrogenation of p-nitrobenzene to aniline [8]. Compared with Pt_1 SAC and Pt NP catalysts, Pt_2 DACs exhibit better catalytic activity for the reaction, which can be attributed to the fact that Pt_2 not only makes the H_2 reactant easy to activate and dissociate, but also makes the desorption of aniline products easier. Table 1 contains several typical 0D NMNs.

Table 1. Different types of 0D NMNs.

Element	Morphology	Diameter
Pt-Ru [1]	nanoclusters	46.78 nm (overall) 2.67 nm (single)
Pt [1]	nanoclusters	32.85 nm (overall) 3.74 nm (single)
Ru [2]	NPs	1.6 nm
Ag [3]	spherical NPs	18~26 nm
PtS [4]	NDs	2.1 nm, 3.2 nm, 4.5 nm
Pt [9]	NPs	11 ± 6 nm
Ag [9]	NPs	25 ± 4 nm
Au [9]	NPs	32 ± 18 nm
Pd [10]	NPs	3.6 nm
Pt [10]	NPs	4.5 nm
Ag [11]	quantum dots	2~5 nm
Ru [12]	quantum dots	1~5 nm
Ag [13]	spherical NPs	20~40 nm
Pd [14]	cuboctahedrons	8~10 nm
Pd [15]	concave nanocubes	37 nm

2.2. 1D NMNs

A 1D nanostructure refers to a structure with two of the three dimensions between 1 and 100 nm [16]. The AR (defined as the ratio of length to diameter) of a 1D metal nanostructure is the basic parameter. According to their different AR values, 1D nanostructures can be divided into nanorods (NRs) and nanowires (NWs). NRs usually refer to 1D nanostructures with an AR less than 30, while the AR of NWs is usually greater than 100. Additionally, 1D nanostructures could exhibit other variations, including branching (or dendritic) structures, hollow structures, core–sheath structures, core–shell structures, alloy structures, and spatially segmented structures. Branched or dendritic nanostructures can be obtained via the additional growth of NRs or NWs from the surface of the pre-synthesized 1D nanostructures. If the 1D nanostructure has a hollow interior, when the AR is relatively large, nanotubes (NTs) will be obtained. When the second metal is uniformly applied to the entire surface of the 1D nanostructure, depending on the AR, a structure with a core–sheath or core–shell morphology can be obtained. The position-selective overgrowth of the second metal at the end of 1D metal nanostructures can form a structure with segmented morphology.

Unlike their 0D and 2D counterparts, 1D nanostructures provide a unique platform to tailor and utilize the electronic, plasmonic, electrical, mechanical, and thermal properties of metals to suit or achieve various types of applications [17].

The synthesis methods of 1D NMNs mainly include the template-assisted method, hydrothermal/solvothermal method, epitaxial growth method, and CO-limited growth method. Sun et al. synthesized porous Pt-Au-Ag NTs via the template-assisted method [18]. As shown in Figure 2a, the as-prepared porous Pt-Au-Ag NTs were synthesized using Au@Ag NRs as sacrificial templates and $PtCl_4^{2-}$ as the replacement reagent. The product achieved a structural change from nanosheets (NSs) to hollow NRs, and finally to porous NTs, which is demonstrated in Figure 2b. Zhang et al. successfully synthesized CPT Rh nanobranches (NBs) via a simple solvothermal method. The CPT Rh NBs are self-supported NBs built with cyclic penta-twinned (CPT) NRs as subunits [19]. It can be seen from Figure 2c that these CPT Rh NBs are composed of multiple NRs with different lengths radiating from the center in different directions. The diameters of NDs are about 4.3 ± 0.6 nm. Xu's group fabricated ultrathin single-crystalline Pd NWs via a template-assisted method [20]. Only H_2PdCl_4, and H_2O were used in the synthesis process. Figure 2d shows that the diameter of Pd NWs was about 3.5 nm, and the individual NWs are very straight and the surface looks smooth. In addition, other Pd nanostructures can be synthesized by changing the aging temperature. This shows that the self-assembly process

strategy of some special surfactants is very much worthy of consideration in the fabrication of NMNs with different morphologies and sizes. Liu et al. used 2D 2H/fcc gold NSs as templates to grow 1D Rh NRs via epitaxial growth [21]. Table 2 contains several typical 1D NMNs.

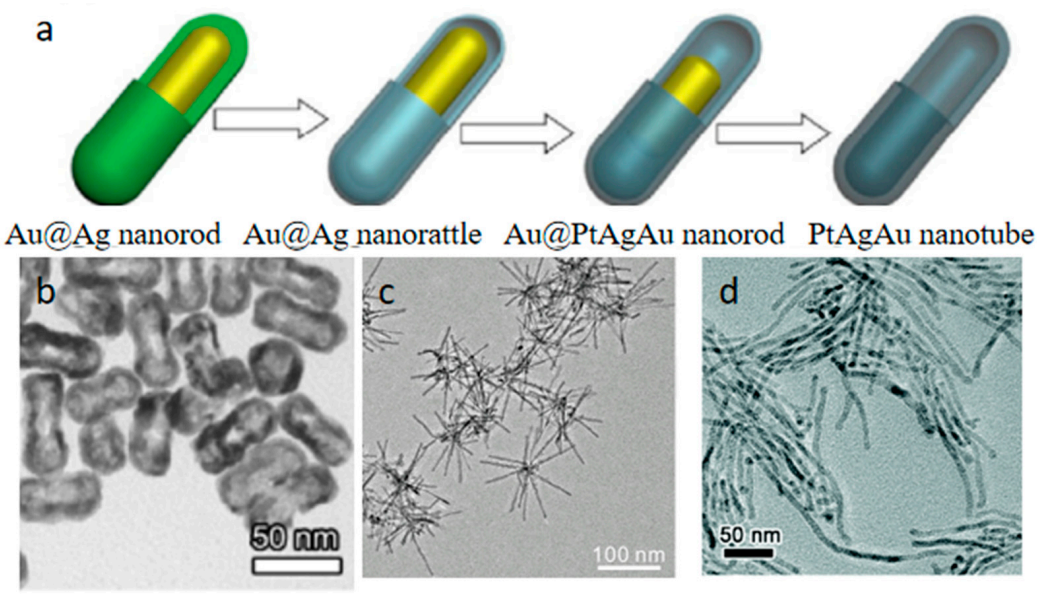

Figure 2. (**a**) Schematic illustration for the synthesis of Pt-Au-Ag NTs. Reprinted from [18] with Permission from Springer Nature, 2016; TEM images of (**b**) Pt-Au-Ag NTs. Reprinted from [18] with Permission from Springer Nature, 2016, (**c**) CPT Rh NBs. Reprinted from [19] with Permission from ACS, 2018, and (**d**) ultrathin single-crystalline Pd NWs. Reprinted from [20] with Permission from RSC, 2016.

Table 2. Different types of 1D NMNs.

Element	Morphology	Diameter
Pt-Au-Ag [18]	porous NTs	
Rh [19]	CPT NBs	4.3 nm
Pd [20]	NWs	3.5 nm
Au [22]	NWs	2.7 nm
Au-Ag [22]	NWs	3.3 nm
Au@Pt [23]	core–shell NWs	6.8 nm
Rh [21]	NRs	
PtM (M=Co, Ni) [24]	mesoporous NTs	100 nm
RuTe [25]	NTs	14 nm
PtCoNiRh [26]	ultrathin nanowires	1.5 nm
Pt [27]	ultrafine jagged nanowires	2.2 nm
Pt-Zn [28]	zigzag-like NWs	6.24 nm
Au–Cu–M (X=Pt, Pd, Ag) [29]	NRs	
Au@Pd@Pt [30]	core–shell NRs	49 nm
Au@Pt [31]	hybrid nanorods	17 nm

2.3. 2D NMNs

A 2D nanostructure refers to a structure with only one of the three dimensions between 1 and 100 nm, including NSs, nanoplates, and ultrathin 2D structures. We can divide 2D nanomaterials into two types: layered structural nanomaterials and non-layered structural nanomaterials. For layered nanomaterials, the in-plane atoms in each layer are interconnected by strong chemical bonds, and these layers are stacked together by weak van der Waals interactions to form bulk crystals. Non-layer structural nanomaterials crystallize in the 3D direction through atoms or chemical bonds to form bulk crystals. In particular,

they can be crystallized into various crystalline phases according to the coordination mode between atoms, the arrangement of atoms, or the stacking sequence between layers. It is worth noting that 2D NMNs are non-layered structures due to metal bonds.

Due to the high aspect ratio, unique surface chemistry, and quantum size effect, 2D nanomaterials usually have rich active sites, significant electronic effects, and strain effects.

Unlike intrinsic layered materials, most metals have highly symmetrical lattices [32]. This indicates that the 2D morphology is not thermodynamically favorable during the growth of noble metal nanocrystals [33]. Therefore, in order to promote 2D anisotropic growth, the growth path is usually dynamically controlled by slowing down the atom addition process or reducing the total free energy of the metal nanostructure [34]. The synthesis methods of 2D noble metal nanomaterials are mainly divided into top-down and bottom-up strategies. On this basis, further distinctions have been made according to the types of key reactants or key experimental conditions. The methods based on the bottom-up synthesis strategy include organic ligand-assisted growth, small-molecule- and ion-mediated synthesis, 2D template-confined growth, the polyol method, seed growth, photochemical synthesis, the water/solvothermal method, crystal phase transition, etc. The methods based on the top-down synthesis strategy include the mechanical compression method, the exfoliating method, nanolithography, etc. As shown in Figure 3a, Huang et al. prepared ultrathin dendritic PdAg nanoplates via the wet chemical method [35]. The lateral size distribution of a single nanoplate was 50–70 nm, and the average thickness was about 1.7 nm, corresponding to about nine atomic layers. It also showed a myriad of curved edges and low-coordination sites. Liu et al. prepared 2H/fcc heterogeneous Au NSs via a facile one-pot method [21]. These Au NSs had a square-like shape, with some of the edges being non-straight and some of the corners truncated. Moreover, their edge length was 416 ± 160 nm, and their thickness was ~8 nm. Liu et al. synthesized ultrathin Pt NSs with a controllable surface structure via a template-assisted method [36], which is shown in Figure 3b. The ultrathin Pt nanoplates were single crystals exposing exclusive {111} facets. Moreover, the thickness of the double Pt layer in the ultrathin Pt nanoplates could be estimated to be ~2 nm, which is approximately seven to nine layers of atoms along the {111} direction. By controlling the time of seeded growth and using the different Ag templates, the thickness and size of the ultrathin Pt NSs could be facilely tailored, respectively. Huang et al. synthesized freestanding ultrathin Pd NSs via a CO-limited growth method [37]. Owing to the growth confinement effect of the CO, the thickness of the palladium NSs could decrease to 1.8 nm—less than 10 atomic layers thick, and the dominant exposed surfaces were {111} facets. Yang's group developed a co-reduction method to synthesize ultrathin PdCu alloy NSs with various Cu/Pd atomic ratios under mild experimental conditions [38]. These PdCu alloy NSs had a thickness of 2.8 ± 0.3 nm, and both Pd and Cu showed homogeneous distributions in the obtained NSs. Figure 3c,d are the TEM images of freestanding ultrathin Pd NSs and PdCu alloy NSs, respectively. Hu et al. synthesized 2D ultra-thin monoatomic Pt layers (PtMALs) using a ligand regulation strategy [39]. They used organic ligand layers to stabilize PtMAL, which were only 0.4 nm thick, equated with an atomic layer thickness. A similar strategy can be extended to the fabrication of monoatomic Au layers and monoatomic Ag layers. Table 3 contains several typical 2D NMNs.

Table 3. Different types of 2D NMNs.

Element	Morphology	Thickness
PdAg [35]	nanoplates	1.7 nm
Au [21]	NSs	8 nm
Pt [36]	nanoplates	2 nm
Pd [37]	NSs	1.8 nm
PdCu [38]	NSs	2.8 ± 0.3 nm
Pt [40]	ultimate thin NSs	1.55 nm

Table 3. *Cont.*

Element	Morphology	Thickness
Ag [41]	high-density NSs	20 nm, 50 nm
Ag [42]	ultrathin and dense NSs	11 nm
Pd [43]	porous nanoplates	10 nm
RhCo [44]	ultrathin NSs	1.3 nm
Rh [45]	hierarchical ultrathin NSs	
Pt@Au [46]	core–shell nanorings	41 nm
AgAu [47]	porous nanomeshes	3 nm
Pd@Au [48]	core–shell nanoplates	4 nm

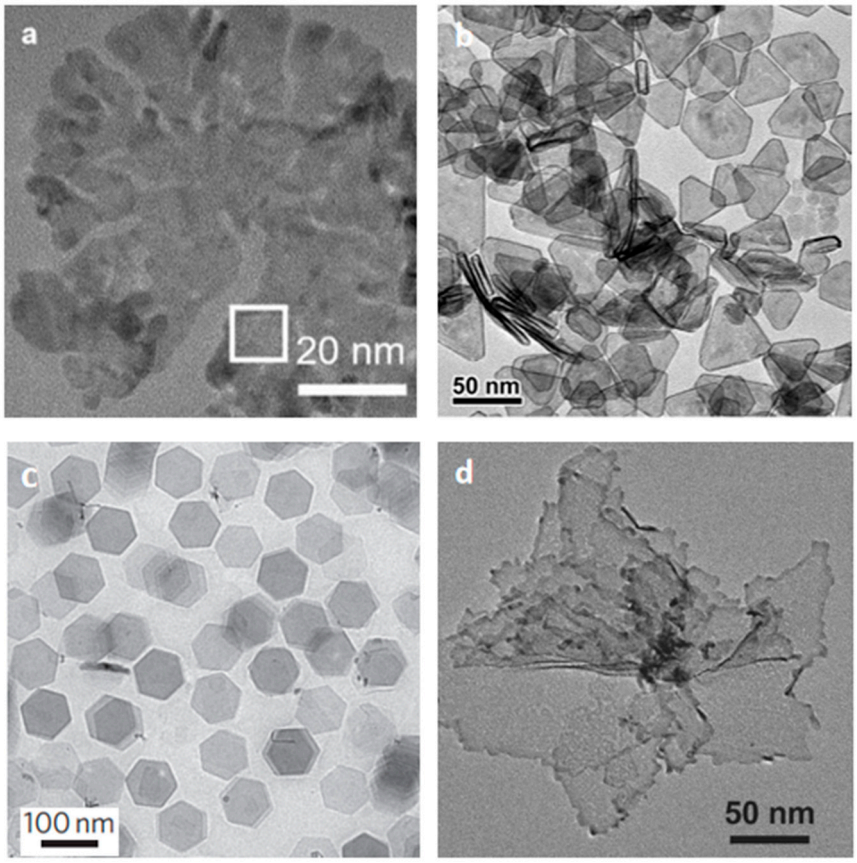

Figure 3. TEM images of (**a**) ultrathin PdAg nanoplates. Reprinted from [35] with Permission from WILEY, 2023, (**b**) ultrathin Pt NSs. Reprinted from [36] with Permission from RSC, 2018, (**c**) freestanding ultrathin Pd NSs. Reprinted from [37] with Permission from Springer Nature, 2018, and (**d**) PdCu alloy NSs. Reprinted from [38] with Permission from WILEY, 2017.

2.4. 3D NMNs

A 3D nanomaterial is composed of one or several types of 0D, 1D, and 2D nanomaterials as basic units, which are arranged or combined in 3D space. The 3D NMs mainly include nanonetworks, nanoaerogels, hollow nanospheres, and so on. A 3D NMN integrates different components into a hybrid nanosystem, using synergistic effects to improve material properties. A 3D NMN often exhibits better structural stability and tunability than other low-dimensional NMNs due to its larger size and more complex solid structure. A 3D NMN still has the characteristics of quantum effect, size effect, and surface effect given by nanostructures and can realize the synergistic modulation of physical properties such as electron transport and coupling, spin polarization, excitation behavior, and wavefront control, and can obtain new characteristics that low-dimensional nanostructures do not have.

The main synthesis methods of 3D NMNs include the hydrothermal/solvothermal method, the ligand-directed method, the template-assisted strategy, the epitaxial growth method, etc. As shown in Figure 4a, Yan et al. successfully synthesized ternary Ag_2S-Au-hPt nanocomposites with solid-state interfaces through a hybrid strategy [49]. Firstly, the core–shell Ag@Pt NPs were prepared using a seed-mediated growth method at elevated temperature. The size of these core–shell Ag@Pt NPs was uniform, and the overall average size was 12.6 nm. Then, under the effect of sulfur, the core–shell Ag@Pt NPs were transformed into Ag_2S-hPt hybrid nanodimers, which were composed of Ag_2S and Pt NPs with a complete hollow interior. As Au was deposited on the surface of the Ag_2S domain, a ternary Ag_2S-Au-hPt nanocomposite was finally formed. In most cases, Au NPs with an average diameter of 8.3 nm were only deposited at a single site on the Ag_2S domain in each Ag_2S-hPt hetero-dimer. It can be seen from Figure 4b that Au and Pt components were, respectively, concentrated on the left and right sides of the nanomaterials, while Ag and S components were concentrated only in the core region. Chen et al. synthesized 3D Pd_3Co and 3D Pd_3Ni nanoassemblies using a simple hydrothermal/solvothermal method [50], as is schematically illustrated in Figure 4c. Figure 4d shows the TEM image of Pd_3M nanoassemblies. The obtained Pd_3M (M=Co and Ni) nanoassemblies all exhibited a typical 3D structure. Arginine needed to be used in the synthesis process, which made it easy to build the highly alloying nanoassemblies via modulating both the nucleation and crystal-growth kinetics. The average particle size of Pd_3Co nanoassemblies was estimated to be about 44.9 nm, and there were many crystal defects on their surfaces, such as dislocation and low-coordinate atomic steps. As shown in Figure 4e, Qiu et al. successfully fabricated a variety of Pt-based alloy NPs through a new synthesis strategy [51]. This novel synthetic strategy uses inorganic molten salts as solvents and does not require the use of any organic surfactants or capping agents. Compared with traditional organic methods, it has many obvious advantages, such as recyclability, low cost, and environmental friendliness. Using this method, they successfully synthesized core–shell PtPd nanocubes (NCs), PtCu NCs, and PtPdCu NCs. In the core–shell PtPd NCs, Pd was concentrated in the core, and Pt was concentrated in the shell region. Figure 4f–h show the TEM images of PtPd NCs, PtCu NHCs, and PtPdCu NCs, respectively. The alloy PtCu NCs comprised single-crystal structures, with an average side length of 26.54 nm. The alloy PtPdCu NCs also showed a single-crystal structure, with an average side length of 40.86 nm. Yoo et al. synthesized truncated octahedral (TOh) PtAu nanoframes (NFs) through a site-specific deposition strategy and fabricated a 3D PtAu nanoframe superstructure via a self-assembly strategy [52]. The average diameter of a single TOh PtAu NF was 72 ± 2 nm, the edge thickness was 14 ± 1 nm, and the pore size was 25 ± 3 nm. Moreover, TOh PtAu NF had a very rare coexistence phenomenon of a double-crystal structure, which meant that one side was pure Pt, and the other side was PtAu alloy. The 3D PtAu NFs exhibited significant long-range order and compactness. Table 4 contains several typical 3D NMNs.

Table 4. Different types of 3D NMNs.

Element	Morphology	Size
Ag@Pt [49]	core–shell NPs	12.6 nm
PtCu [51]	NCs	26.54 nm
PtPdCu [51]	NCs	40.86 nm
PtAu [52]	TOh NFs	72 ± 2 nm
Pd_3Co [50]	nanoassemblies	44.9 nm
Au@Pd [53]	core–shell NPs	10.14 nm
Ru@Pd [53]	core–shell NPs	11.36 nm
Au@AgPt [54]	complex hexoctahedral NPs	
Pd-M (M=Ag, Pb, Au) [55]	NSs with tremella-like superstructures	
Au/Ag/Pd [56]	self-assembled aerogel	4.8 nm

Table 4. *Cont.*

Element	Morphology	Size
PtPd [57]	aerogel	4.9 nm
Pt-Ru [58]	assembled aerogel	
Pt-Ni-Co [59]	nanoframe crystals	20 nm

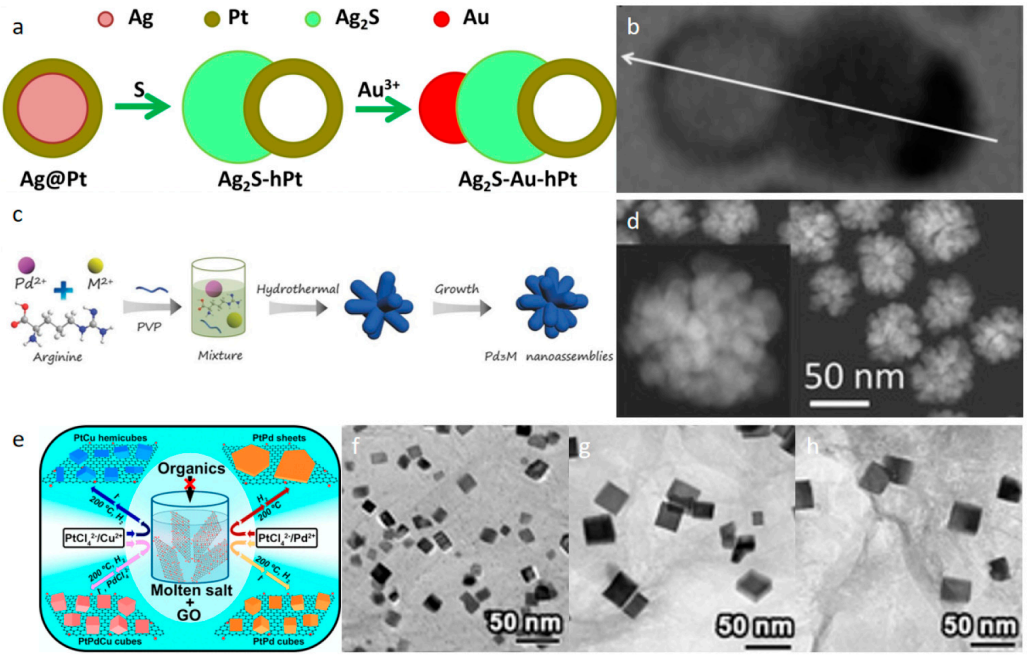

Figure 4. (**a**) Schematic illustration for the synthesis of ternary Ag_2S-Au-hPt nanocomposites using core-shell Ag@Pt NPs as the starting templates; (**b**) TEM image of a single particle of the ternary Ag_2S-Au-hPt nanocomposites. Reprinted from [49] with Permission from Springer Nature, 2014; (**c**) schematic illustration of the formation of Pd_3M nanoassemblies; (**d**) TEM image of Pd_3Co nanoassemblies. Reprinted from [50] with Permission from WILEY, 2018; (**e**) illustration of the synthesis of PtPd NCs/RGO, PtCu NHCs/RGO, and PtPdCu NCs/RGO in inorganic molten salt with the assistance of GO; TEM images of (**f**) PtPd NCs, (**g**) PtCu NHCs, and (**h**) PtPdCu NCs. Reprinted from [51] with Permission from ACS, 2017.

3. The Structure–Activity Relationship of NMNs

In different catalytic systems, due to the differences in lattice planes, edges, and angles exposed by nanomaterials of different dimensions, the thermodynamic and kinetic processes of reaction substrates, active intermediates, and products on the catalyst surface are different. Thus, dimension engineering plays various roles in different catalytic reactions. In addition, the microscopic factors that determine the performances of nanocatalysts in different dimensions are very complicated and diverse.

In some catalytic systems, when a certain structural characteristic of the 0D nanocatalyst is changed, its catalytic activity will change accordingly. Crystal orientation is an important factor affecting 0D nanocatalysts. Chen et al. loaded Ru nanoparticles with an fcc structure and hcp structure on γ-Al_2O_3 [60]. The results show that the hcp Ru/γ-Al_2O_3 had better catalytic activity than the fcc Ru/γ-Al_2O_3 under the condition of similar Ru size. By changing the crystal orientation of the catalyst, the crystal plane exposed in the catalytic system contained more active sites, thereby improving the catalytic activity of the catalyst. The grain size is also an important factor affecting 0D nanocatalysts. As the particle size of the catalyst decreases, the active surface area of the material exposed to the catalytic reaction increases, which, in turn, increases the catalytic activity. This phenomenon is called the size effect, and it is most pronounced in 0D nanocatalysts. Tanabe et al. used Au

nanospheres of different sizes (5–60 nm) to modify TiO_2 photocatalysts [61]. The attenuated total reflection spectroscopy measurement showed that the Au nanospheres with smaller particle size aroused greater spectral changes, which meant greater electronic state changes and higher charge separation efficiency enhancement. In fact, TiO_2 modified by smaller Au nanospheres showed higher photocatalytic activity. Moreover, Au NRs or Au NCs with different aspect ratios are deposited on TiO_2, but their spectra did not change significantly.

The 1D nanocatalysts provide a unique platform to tailor and utilize distinct plasmonic, electrical, mechanical, and thermal properties to regulate various catalytic systems. Si et al. successfully synthesized a NWs/C catalyst and Pt NPs/C catalyst [62]. Electrochemical tests demonstrate that compared with Pt NPs nanocatalysts, Pt NWs nanocatalysts have a higher electrochemical surface area, higher CO resistance, and higher electron transfer coefficient. Due to the larger continuous surface and more active sites of Pt NWs, they have a larger hydrogen adsorption/desorption peak area and stronger adsorption capacity in dimethyl ether electrooxidation reaction. AR is one of the most important factors affecting the 1D nanocatalysts. Zhou et al. fabricated three kinds of Au NRs with different AR (AR = 2.8, 3.3, 3.8) [63]. The catalytic results show that the Au NRs with larger AR had higher catalytic activity. Similar conclusions can also be drawn from the literature [61,64–66]. The facet shape is also one of the most important factors affecting the 1D nanocatalysts. The facets, such as cuboid facets, convex cube facets, and concave cube facets, have richer optical extinction spectra, a wider plasma tuning range, and enhanced catalytic tunability compared to the traditional circular facets [67]. In addition, the hollow structure also significantly affects the catalytic activity of 1D nanocatalysts. The 1D hollow structure has obvious advantages over a solid structure. The 1D hollow structure has a poor effect on liquid phase mass transfer and, hence, macropores can be introduced to minimize diffusion resistance, enhance mass transfer, and potentially enhance the distribution of active sites during catalyst preparation [68].

Due to their large specific surface area and unique surface chemistry, 2D nanocatalysts generally exhibit rich active sites, significant electronic effects, and strain effects, which could be applied in specific catalytic reactions. Sadeghi et al. fabricated spherical Ag NPs and Ag NSs with different sizes on the surface of zinc oxide tin (ZTO) [69]. Ascorbic acid oxidation tests are carried out on the two electrodes. It was observed that the peak current of the ZTO electrode modified by Ag NSs was almost two to three times higher than that of the ZTO electrode modified by spherical Ag NPs. Compared with the ZTO electrode modified by spherical Ag NPs, the ZTO modified by Ag nanosheets has higher catalytic activity. Ag NSs have more sharp edges, which exhibit higher catalytic activity than flat areas. In addition, the electrode active region is also an important factor affecting the electrocatalytic activity. The size of the spherical NPs is small and does not exceed the size of the diffusion layer, which does not contribute much to the area of enhanced electrocatalytic activity, so the electrocatalytic activity of Ag NPs is not as good as that of Ag NSs. When the thickness of the 2D nanomaterial is reduced to a certain extent (<5 nm), the electrons can be confined to the ultra-thin region and, hence, the electrons will easily move along the 'ab plane' of the two-dimensional sheet. This also has a significant effect on the electrocatalytic performance of 2D nanomaterials.

The 3D nanocatalysts based on combination of different structures could significantly magnify the synergistic effects and, hence, improve the catalytic performance in specific catalytic systems. Bukhtiyarov et al. found that the Au-shell-Pd-core nanocatalysts exhibited higher pairwise selectivity than the PdAu alloy nanocatalysts [70]. The reason is that the core–shell structure enhances the dilution effects of Au atoms on Pd sites, and the dilution effects are positively correlated with catalytic performance. Yoo et al. synthesized truncated octahedral (TOh) PtAu nanoframes (NFs) through a site-specific deposition strategy, and fabricated a 3D PtAu nanoframe superstructure via a self-assembly strategy [52]. TOh PtAu NF has a very rare coexistence phenomenon of a double-crystal structure, which means that one side is pure Pt and the other side is PtAu alloy. The 3D PtAu NFs exhibit significant long-range order and compactness. Compared with solid NPs, the unique nanoframe

superstructure has efficient mass transport and maximum exposed surface area. These advantages mean that it exhibits a better diffusion rate, higher catalytic activity, and better selectivity for catalytic reactions.

4. Applications

4.1. Direct Alcohol Fuel Cells (DAFCs)

Due to the empty d orbital, noble metals can efficiently form coordination bonds to participate in the reaction. Noble metal nanocatalysts have the advantages of easy adsorption of reactants on the surface, good chemical activity, and good stability, and have a very broad application prospect in the field of fuel cells. This section mainly introduces DAFCs and focuses on the alcohol oxidation reaction (AOR).

The AOR refers to the electro-oxidation reaction of methanol, ethanol, ethylene glycol, and other alcohol fuels, which constitutes the anode reaction in DAFCs. Pt-based nanomaterials are commonly used in the production of DAFCs due to the good catalytic activity of Pt for the alcohol oxidation reaction. Moreover, Pd- and Ru-based nanomaterials have good electronic and proton conductivity, and have a high catalytic efficiency for the alcohol oxidation reaction in alkaline media. Therefore, Pd and Ru-based nanomaterials are also commonly used in the production of DAFCs. Tan Qiang prepares a core–shell Au@Pd nanocatalyst using a three-phase phase transfer method. The catalyst has higher catalytic activity and stability for the oxidation of methanol in alkaline medium. When the ratio of shell Pd to core Au is 5:1, the catalytic activity of the catalyst is the highest. The Au@Pd catalyst showed higher stability than the traditional pure Pd catalyst. After 1000 cyclic voltammetry aging tests, the active area decreased by only 5.9%, while the active area loss rate of the pure Pd catalyst in the same medium was 70.8%. The results of XPS and computational chemistry show that the electronic interaction between the Au@Pd shell and the core leads to the shift of the d-band center of the Pd shell, which is the reason for the high activity and stability of the catalyst. Gao at el. developed a versatile, surfactant-free, and simple one-pot method for the precise synthesis of a novel self-supporting Pd-M (M=Ag, Pb, Au, Ga, Cu, Pt) NSs with a tremella-like superstructure assembled from ultrathin 2D NSs [55]. The Pd-M (M=Ag, Pb, Au) NSs with a tremella-like structure exhibit an excellent ethanol oxidation reaction (EOR) and ethylene glycol oxidation reaction (EGOR) performance. In particular, the EOR/EGOR mass activities of Pd_7Ag NSs, Pd_7Pb NSs, and Pd_7Au NSs are 8.2/7.3, 7.2/5.7, and 5.3/4.4 times that of commercial Pd/C catalysts, respectively, under the optimal superstructure, better electronic effect and promoted toxicity tolerance. This advanced 3D construction also gives Pd-M NSs more favorable stability than Pd/C. This study may be extended to Pd-M (M = other metals) NSs, opening up more opportunities for a wide range of catalytic applications. Wei et al. used a novel epitaxial growth strategy to synthesize RuTe/M (M=Pt, Pd, PdPt, PdAu) NTs, which have high quality and a high aspect ratio [25]. The RuTe/M NTs exhibit high mass activity for methanol/ethanol electrooxidation, which is much higher than that of commercial catalysts. It is potential for them to be an efficient and widely used anode catalyst for fuel cells. All the RuTe/M NTs have higher peak current values than commercial Pt/C. In particular, the positive peak current densities of RuTe/PdAu NTs and RuTe/PdPt NTs are, respectively, 4.6 and 4.2 A mg^{-1} metal, four times better than that of commercial Pt/C.

4.2. Hydrogen Fuel Cells

With the increasing global warming and air pollution, traditional fuel vehicles no longer meet the conditions of green development. We urgently need to develop a new type of fuel cell technology. The main reaction involved in hydrogen fuel cells is the redox reaction (HOR) of hydrogen, which is the reverse reaction of the electrolysis of water to produce hydrogen and oxygen. Since the product is only water, the hydrogen fuel cell is an environmentally friendly battery. In general, hydrogen fuel cells use a proton-exchange membrane fuel cell (PEMFC) and an anion-exchange membrane fuel cell (AEMFC) technologies. Catalysts are the core components of proton-exchange membranes

and anion-exchange membranes. Pt and Pd have been widely used in the production of commercial hydrogen fuel cells. PEMFC often uses Pt-based catalysts, and AEMFC often uses Rh-based and Pd-based catalysts. They have high catalytic activity for HOR and high anti-toxicity. This ensures the long-term stable operation of hydrogen fuel cells. Since commercial PEMFC catalysts are all platinum-based catalysts, the development of hydrogen fuel cells is facing the problem of high cost. Based on this, we can solve this development problem by reducing the amount of noble metals such as platinum or by seeking low-cost alternative materials.

Elbert at el. synthesized Ru@Pt core–shell and single-crystalline NPs, with a sharp and ordered interface [71]. By coating Pt on Ru cores, they prepared the $Ru_1@Pt_{0.5}$(1ML)/C and $Ru_1@Pt_1$(2ML)/C catalysts, respectively, with dominant one- and two-monolayer Pt shells. The HOR–HER activities of both Ru@Pt core–shell/C catalysts were better than those of commercial Pt/C and RuPt/C catalysts. The core–shell catalysts exhibited enhancement factors of Pt mass HOR–HER activities of 4.0 for $Ru_1@Pt_1$(2ML) and 3.7 for $Ru_1@Pt_{0.5}$(1ML)/C, compared with Pt catalysts. Bellini et al. synthesized a Pd-CeO_2/C catalyst with engineered Pd-to-CeO_2 interfacial contact [72]. The Pd-CeO_2 interfacial contact resulted in better HOR activity in AEMFC tests (>1.4 W cm^{-2} peak power densities). Mao et al. synthesized a novel HOR catalyst, $RuNi_1$, in which Ni was atomically dispersed on the Ru nanocrystals [73]. The $RuNi_1$ catalyst exhibited excellent catalytic activity and stability for HOR in alkaline media, better than Ru-Ni bimetallic nanocrystals, pristine Ru, and commercial Pt/C catalysts. Alia et al. synthesize Pt/Cu NWs with a diameter of 100 nm and a length of 25~40 μm via the partial galvanic displacement of Cu NWs [74]. The area and mass exchange current density of Pt/Cu NWs are 3.5 times and 1.9 times better than that of carbon-supported Pt, respectively. Dhanya et al. synthesized Pt/WO_3 catalyst, in which Pt NPs (≤20 wt%) were uniformly modified on WO_3 NSs [75]. The study revealed that the Pt/WO_3-550 catalyst showed comparable HOR activity to that of commercial Pt/C in terms of limiting current density and onset potential. This showcased that Pt/WO_3, under optimum conditions, could be used as the best alternative for carbon-free electrocatalyst for PEMFCs. Li at el. reported an atomically dispersed Pt catalyst (Pt-C-AA, with Pt 1.70 wt%) containing both Pt single atoms and Pt_4 clusters [76]. It was found to be highly active (1148 mW cm^{-2}) for the HOR in a PEMFC, and also presented remarkable durability and tolerance during the HOR process.

4.3. Water Splitting

As a cathode half-reaction for water splitting to produce hydrogen, the hydrogen evolution reaction (HER) has received extensive attention. Since the $|\Delta G_H^*|$ (Gibbs free energy of hydrogen adsorbed on the metal interface) of platinum is closest to 0 among traditional metals [77], Pt is one of the most efficient catalysts for HER. However, Pt also has high catalytic activity in the HOR. Moreover, for the low catalytic activity of Pt in alkaline electrolytes such as seawater [78], Pt-based catalysts need to be improved via structural regulation or heteroelement doping. Li et al. synthesized PtNiP MNs through a facile Ni, P co-incorporation strategy [79]. Benefiting from the unique mesoporous structure and the changes in electronic structure and composition brought by metal-nonmetal ternary alloys, PtNiP MNs exhibit excellent activity and durability for the HER, the oxygen evolution reaction (OER), and overall water splitting.

Rhodium is considered to be one of the most promising candidates because its activity in alkaline media is only one order of magnitude lower than that in acidic systems. Zhang et al. synthesized Rh nanocrystals with different structures, including tetrahedron (TH), concave tetrahedron (CT), and nanosheet (NS), and further measured the catalytic activity of these Rh nanocrystals for the HER [80]. By measuring the HER polarization curves of the three catalysts under 0.1 M KOH, it can be found that the overpotential of Rh NS at a current density of 10 mA cm^{-2} is 0.043 V lower than that of Rh/C. The overpotential of Rh/C catalyst increased sharply to 0.193 V after electrolysis for 5 h, while the overpotential of Rh NSs increased slightly to 0.065 V, which was much lower than that of the Rh/C catalyst.

These results demonstrate the crucial function of structural regulation in improving catalyst performance. The preparation of Rh NP/C catalyst by combining Rh NPs with C support can also improved the performance of the catalyst [81].

In addition to the electrocatalytic decomposition of water to produce hydrogen, the use of sunlight to decompose water to produce hydrogen has also received great attention. Noble metals, including Pt, Au, Ag, etc., can be used as cocatalysts to improve the photocatalytic efficiency of the HER by compounding with a TiO_2 photocatalyst. Unlike other catalytic reactions, Pt^0 NPs have little contribution to the photocatalytic HER, but the oxidized Pt species embedded on the surface of TiO_2 comprise the key active site [82]. Moreover, Li et al. found that controlling the valence state of Pt could unidirectionally inhibit the reverse reaction of the HER, thereby improving the solar energy conversion efficiency [83]. NMNs such as Ag, Rh, and Au could also be used in photocatalytic hydrogen production [84–86].

4.4. Selective Hydrogenation Reaction

A selective hydrogenation reaction refers to the process in which the target functional group is hydrogenated and the other functional group is not affected when the reactant contains two unsaturated functional groups. The selective hydrogenation reaction has a very wide range of applications in the chemical industry, including the production of fine chemicals and petrochemicals and drug synthesis. Since the traditional nanocatalysts are prone to complete hydrogenation, it is a great challenge to obtain the target product with high selectivity.

Taking the selective hydrogenation of α, β-unsaturated aldehydes to unsaturated alcohols as an example, Pd- or Pt-based noble metal hydrogenation catalysts tend to first hydrogenate C=C to form saturated aldehydes, and then further convert the products to saturated alcohols. The Ag-based catalyst has a unique ability to first hydrogenate the C=O bond without destroying the C=C bond [87]. This indicates that we can improve the selectivity of the target reaction by selecting the appropriate metal.

In addition, without changing the composition of noble metal catalysts, dimensional regulations can also change the hydrogenation path and improve the selectivity of noble metal catalysts. As shown in Figure 5a,b, Wei et al. reported a remarkable phenomenon whereby noble metal NPs (Pd, Pt, Au-NPs) could be transformed into thermally stable single atoms (Pd, Pt, Au-SAs) above 900 °C in an inert atmosphere [88]. Figure 5c shows that for the semi-hydrogenation of acetylene, Pd-SAs exhibited better activity and selectivity than Pd NPs. As shown in Figure 5d,e, Xu et al. synthesized two types of Pt-based nanocatalysts on a $CoAlO_x$ support, including single-atom $Pt_1/CoAlO_x$ catalysts and nanocluster $Pt_n/CoAlO_x$ catalysts [89]. Figure 5f indicates that $Pt_1/CoAlO_x$ showed >99% selectivity for furfural (FAL) hydrogenation to furfuryl alcohol (FOL), while $Pt_n/CoAlO_x$ showed >99% selectivity for FAL hydrogenation to tetrahydrofurfuryl alcohol (THFOL).

Moreover, the combination of noble metals with other metals can also significantly improve their catalytic selectivity. Takato et al. synthesized a core-Pd/shell-Ag nanocomposite catalyst, which could achieve the highly selective semihydrogenation of alkynes [90]. Figure 5g,h show the TEM image and elemental mapping image of the core-Pd/shell-Ag nanocomposite catalyst. Core-Pd is used for the hydrogenation of alkynes, and shell-Ag effectively inhibits the excessive hydrogenation of olefins. The complementary relationship between core-Pd and shell-Ag causes it to exhibit high activity and high selectivity in the semi-hydrogenation of alkynes, which is shown in Figure 5i. Chen et al. fabricated a Pt-Ni/γ-Al_2O_3 catalyst, which is composed of Pt NPs with surrounding Ni atoms and supported on γ-Al_2O_3 [91]. Different from the hydrogenation of CO_2 by Pt/γ-Al_2O_3 and Ni/γ-Al_2O_3, the Pt-Ni/γ-Al_2O_3 catalyst can hydrogenate CO_2 to formate and further hydrogenate to CH_4. This is because the presence of Pt-Ni bimetallic sites changes the hydrogenation path, on which the electronic interaction between Pt particles and surrounding Ni atoms promotes the further hydrogenation of formate species to CH_4. Wang et al. synthesized bimetallic Pd-Au NPs supported on carbon NTs, which had high selectivity

for the hydrogenation of phenylacetylene to styrene [92]. Combining noble metals with other metals can change the electronic structure of their surfaces, which will affect the adsorption of the reaction substrate by the catalyst, resulting in different selectivity in the hydrogenation reaction.

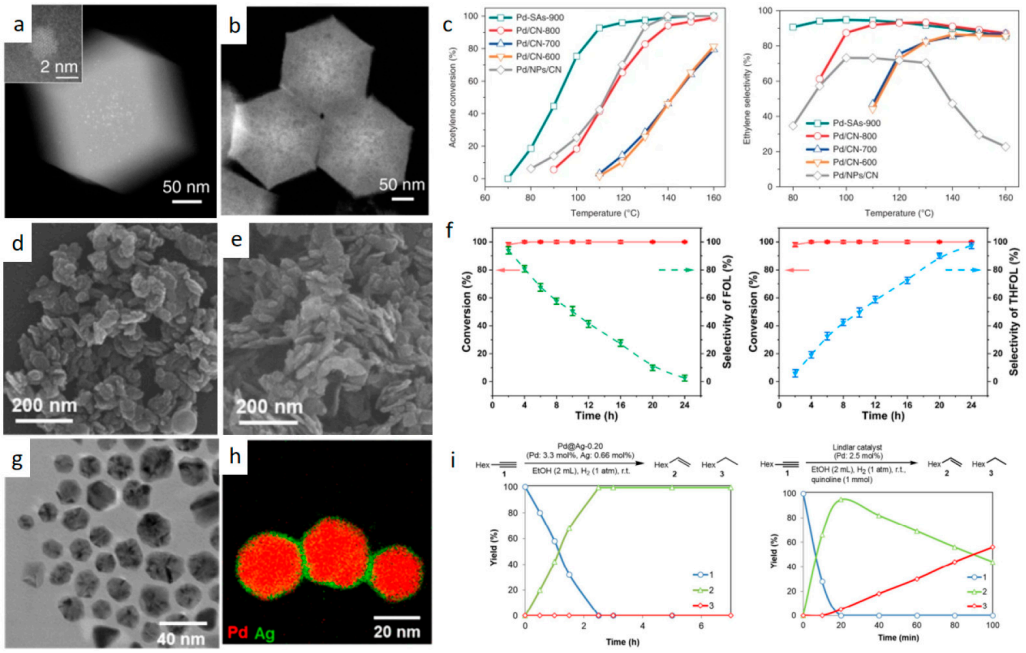

Figure 5. TEM images of (**a**) Pd NPs and (**b**) Pd single atoms; (**c**) acetylene conversion and ethylene selectivity of Pd-SAs and Pd-NPs. Reprinted from [88] with Permission from Springer Nature, 2018; SEM images of (**d**) $Pt_1/CoAlO_x$, and (**e**) $Pt_n/CoAlO_x$; (**f**) FOL selectivity of $Pt_n/CoAlO_x$, and THFOL selectivity of $Pt_n/CoAlO_x$. Reprinted from [89] with Permission from ACS, 2023; (**g**) TEM image and (**h**) elemental mapping image of core-Pd/shell-Ag catalyst; (**i**) time profile of semihydrogenation of Pd@Ag and Lindlar catalyst. Reprinted from [90] with Permission from ACS, 2016.

4.5. Treatment of Automobile Exhaust

Automobile exhaust has always been a major problem restricting environmental protection. Automobile exhaust contains a large number of harmful substances, including carbon monoxide (CO), hydrocarbons (HCs), nitrogen oxides (NO_X) and so on. A high-performance ternary catalyst (TWC) is a catalyst that can simultaneously purify three pollutants of carbon monoxide (CO), hydrocarbons (HCs), and nitrogen oxides (NO_X). It is the most important part of the automobile exhaust system. At present, TWC catalysts are mainly composed of Ru, Rh, and Pd as active components, and Al_2O_3, CZ (ceria-zirconia-based oxide), and other materials as carriers to prepare composite catalysts [93].

The structure of the catalyst is one of the most important factors affecting the performance of the catalyst. The preparation of TWC catalysts with different structures without changing the composition of the catalyst can improve the catalytic efficiency of TWC. Mahara et al. successfully synthesized a $Co@Ru/Al_2O_3$ catalyst for automotive ternary reaction via galvanic deposition (GD) as a bimetallization method [94]. As shown in Figure 6a, Ru is concentrated in the shell, and Co is concentrated in the core, and only a small part of Ru and Co form an alloy at the interface. Moreover, since Ru forms a shell on Co, its electronic state changes, and a step surface with large Ru particles appears, which means that Rh still has high catalytic activity for NO_x in the low temperature range. Figure 6b is the NO-C_3H_6-CO-O_2 reaction test diagram of Co@Ru-GD, Ru/Co-seq, Ru-imp, and Co-imp. It can be found that the NO conversion on Co@Ru-GD decreased by about 50 °C compared with the other three catalysts. Le et al. prepared macroporous TWC particles via a template-assisted method using a precursor solution containing TWC NPs and PSL as templates [95]. From Figure 6c, it can be seen that TWC NPs are irregular in shape, with an

average particle size of 10 ± 3 nm. The aggregate TWC particles are spherical and have mesopores with an average diameter of 10 nm on the surface. The macroporous TWC particles prepared using PSL as a template are also spherical. The TWC aggregate and macroporous TWC particles have the same particle size, of about 700 nm. CO oxidation was selected as a model reaction to evaluate the performance of TWC particles with different structures, and macroporous TWC NPs exhibit the best CO catalytic activity. As is shown in Figure 6d, the improved convective diffusion within the particles facilitates the contact between reactants and the interior catalyst surface, thereby enhancing the overall catalytic performance. Li et al. compare the $Pd@CeO_2/Al_2O_3$ core–shell catalysts and $Pd/CeO_2/Al_2O_3$ catalysts for the ternary reaction [96]. The results show that the T_{90} values of CO, HC oxidation, and NO reduction over the $Pd@CeO_2/Al_2O_3$ core–shell catalysts were 40, 80, and 40 °C lower than those over the $Pd/CeO_2/Al_2O_3$ catalysts, respectively. This indicates that the preparation of materials with a core–shell structure is an effective method of improving the catalytic performance of materials without changing the composition of the catalyst.

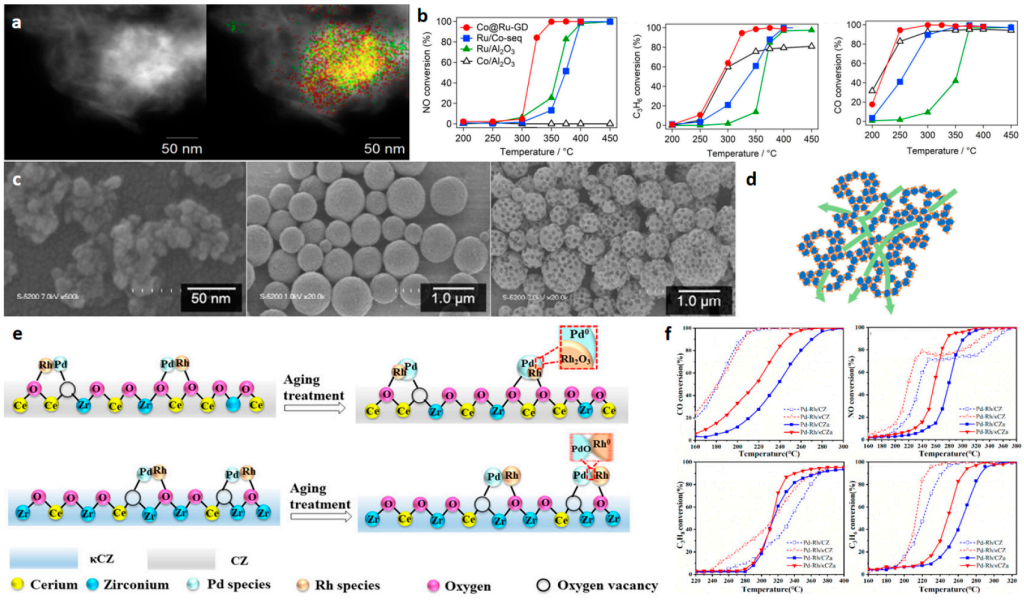

Figure 6. (**a**) Typical HAADF-STEM images and those overlaid with Ru and Co EDS elemental maps for Co@Ru-GD; (**b**) NO, C_3H_6, and CO conversions as a function of the reaction temperature for the $NO-C_3H_6-CO-O_2$ reaction over four catalysts. Reprinted from [94] with Permission from WILEY, 2018; (**c**) SEM images of TWC NPs, aggregate TWC NPs, and macroporous TWC NPs; (**d**) the proposed gaseous diffusion mechanisms through macroporous TWC NPs. Reprinted from [95] with Permission from ACS, 2023; (**e**) schematics describing the thermal evolution of noble metal species for Pd–Rh bimetallic catalysts; (**f**) the three-way catalytic performance for C_3H_8, NO, C_3H_6, and CO on Pd–Rh/CZ and Pd-Rh/κCZ. Reprinted from [97] with Permission from ACS, 2022.

In addition, the choice of support also has a great influence on the performance of the catalysts. Yin et al. prepared a κCZ (partial κ-$Ce_2Zr_2O_8$ structure)-supported Pd-Rh [97], the schematic of which is shown in Figure 6e. Figure 6f indicates that, compared with the traditional CZ-supported Pd-Rh catalysts [92], the T_{50} of C_3H_8, NO, and C_3H_6 of Pd-Rh/κCZ catalysts was reduced by 10~20 °C. After thermal aging at 900 °C for 4 h, the T_{90} of C_3H_8, NO, C_3H_6, and CO of Pd-Rh/κCZ catalysts still decreased more than 20 °C. This is because κCZ has a lower oxygen vacancy energy and a Zr-rich surface, and there is more Rh^0 on the catalyst surface, which inhibits the formation of a Pd-Rh alloy, and ultimately achieves an improvement in TWC performance.

5. Challenges and Perspectives

Catalysts play a vital role in industrial production, which is closely related to people's lives and economic development. In recent years, the increasing global carbon dioxide emissions have significantly amplified the severity of global warming and cast great restrictions on people's lives. NMNMs have been widely used as efficient catalysts in the fabrication of DAFCs, hydrogen fuel cells, water splitting, the selective hydrogenation reaction, and the treatment of automobile exhaust. However, most commercial NMNM catalysts are currently facing difficulties that mean that they cannot be used in complex environments. Therefore, we urgently need to develop multifunctional catalysts, that can be used in a variety of conditions. Meanwhile, it is important to find a general synthesis method to reduce the expense of fabricating these catalysts. Improving catalytic efficiency and increasing stability and service life are also the top priorities of catalyst development. Here is a short list of some potential solutions to the challenges:

(1) Exploring general synthesis methods for multifunctional noble-metal-based catalysts. Developing general catalyst fabrication methods including adaptable surface properties and multiple active sites, as well as scalable manufacturing processes, is essential for diversified modern chemical industry. Universal synthetic strategies, such as the hydro/solvothermal approach, ligand-guided method, template-assisted route, epitaxial growth, and CO-confinement strategy, have been reported before. The innovative design of multifunctional catalysts should be versatile enough to satisfy various changing environmental conditions;

(2) Enhancing catalytic efficiency and stability, as well as the service life. Improving the catalytic efficiency and stability of these catalysts is critical. Research should focus on optimizing the catalyst structure at the nanoscale, controlling active site densities, and enhancing the catalyst-support interaction to achieve higher efficiency and long-term stability under varying environmental conditions. Moreover, extending the service life of catalysts will contribute to their economic viability and environmental impact. Strategies such as developing robust protective coatings, designing self-regenerating catalyst systems, or exploring novel materials with inherent durability could be explored to enhance the longevity of these catalysts;

(3) Revealing the intrinsic catalytic mechanism based on in situ analysis technology and simulation calculation. A comprehensive understanding of catalytic reaction mechanism is imperative for the rational design of catalysts with complex configurations and structures. In many cases of experimental research and chemical production, it is necessary to analyze the intermediate products of the reaction. The development of in situ analysis technology enables extensive testing and analysis under conditions closely resembling reality, thereby yielding more precise data and results. Moreover, revealing the surface reconstruction mechanism of the catalyst and correlating it with the distribution of active sites is also vital for improving catalyst activity. The revelation of intrinsic catalytic mechanisms through the use of both in situ analysis technology and simulation calculations is a crucial objective for catalyst manufacturing. In situ XRD and in situ XAF techniques can be used to characterize the dynamic phase changes of the reactants and observe the evolution of catalyst structure and, on this basis, analyze the restructuring phenomenon of the catalyst during the catalytic process. The in situ TEM technique can be used to observe the atomic arrangement on the catalyst surface in real time and further analyze the atomic rearrangement on the catalyst surface. In situ infrared technology and in situ Raman technology are used to observe the formation of active intermediates in the catalytic process in real time, which is very important and efficient in revealing the catalytic reaction mechanism.

Author Contributions: B.L. and H.Y. contributed equally to this work. B.L.: Investigation, Draft Writing, Writing—Reviewing and Editing, H.Y.: Investigation, Draft Writing, Supervision, Writing—Reviewing and Editing, P.H.: Conceptualization, Supervision, Investigation, Writing—Reviewing and Editing, H.Z.: Conceptualization, Supervision, Investigation, Writing—Reviewing and Editing. G.-S.W.: Conceptualization, Supervision, Investigation, Writing—Reviewing and Editing. Y.G.: Conceptualization, Supervision, Investigation, Writing—Reviewing and Editing. All authors have read and agreed to the published version of the manuscript.

Funding: This worked is financially supported by the National Key R&D Program of China (2020YFA0710403, 2020YFA0710404), the Beijing Municipal Science & Technology Commission (221100007422088) and Natural Science Foundation of China (52371147, 52222203, 52073008, U1910208, 52250119).

Acknowledgments: The authors thank all members of the P. H. subject group and Laboratory 606 for supporting this work.

Conflicts of Interest: The authors declare no conflict of interest.

References

1. Li, X.; Qian, C.; Tian, Y.; Yao, N.; Duan, Y.; Huang, Z. Pt-Ru Bimetallic Nanoclusters with Super Peroxidase-Like Activity for Ultra-Sensitive Lateral Flow Immunoassay. *Chem. Eng. J.* **2023**, *457*, 141324. [CrossRef]
2. Cao, Y.G.; Liang, S.; Yan, Y.; Dong, W.J.; Dong, C.L.; Zheng, W.S.; Nong, S.Y.; Huang, F.Q. Unique Sandwich Structure of Ru@TiO_2: Salicylic Acid Micro-Etching from $K_2Ti_2O_5$ and High-Performance Electrocatalytic Hydrogen Evolution. *Inorg. Chem. Front.* **2023**, *10*, 3852–3859. [CrossRef]
3. Fang, L.; Feng, J.J.; Shi, X.B.; Si, T.Z.; Song, Y.; Jia, H.; Li, Y.T.; Li, H.W.; Zhang, Q.G. Turning Bulk Materials into 0d, 1d and 2d Metallic Nanomaterials by Selective Aqueous Corrosion. *Chem. Commun.* **2019**, *55*, 10476–10479. [CrossRef] [PubMed]
4. Li, M.; Wang, Y.; Li, T.; Zhang, J.; Wang, X.; Luo, J.; You, M.; Yang, T.; Deng, Y.B.; Yang, H.; et al. Albumin-templated platinum (II) sulfide nanodots for size-dependent cancer theranostics. *Acta Biomater.* **2023**, *155*, 564–574. [CrossRef] [PubMed]
5. Qiao, B.T.; Wang, A.Q.; Yang, X.F.; Allard, L.F.; Jiang, Z.; Cui, Y.T.; Liu, J.Y.; Li, J.; Zhang, T. Single-Atom Catalysis of Co Oxidation Using Pt_1/FeO_x. *Nat. Chem.* **2011**, *3*, 634–641. [CrossRef] [PubMed]
6. Zhu, Y.F.; Yuk, S.F.; Zheng, J.; Nguyen, M.T.; Lee, M.S.; Szanyi, J.; Kovarik, L.; Zhu, Z.H.; Balasubramanian, M.; Glezakou, V.A.; et al. Environment of Metal-O-Fe Bonds Enabling High Activity in CO_2 Reduction on Single Metal Atoms and on Supported Nanoparticles. *J. Am. Chem. Soc.* **2021**, *143*, 5540–5549. [CrossRef] [PubMed]
7. Mochizuki, C.; Inomata, Y.; Yasumura, S.; Lin, M.Y.; Taketoshi, A.; Honma, T.; Sakaguchi, N.; Haruta, M.; Shimizu, K.; Ishida, T.; et al. Defective Nio as a Stabilizer for Au Single-Atom Catalysts. *ACS Catal.* **2022**, *12*, 6149–6158. [CrossRef]
8. Tian, S.B.; Wang, B.X.; Gong, W.B.; He, Z.Z.; Xu, Q.; Chen, W.X.; Zhang, Q.H.; Zhu, Y.Q.; Yang, J.R.; Fu, Q.; et al. Dual-Atom Pt Heterogeneous Catalyst with Excellent Catalytic Performances for the Selective Hydrogenation and Epoxidation. *Nat. Commun.* **2021**, *12*, 3181. [CrossRef]
9. Jiang, Y.H.; Guan, L.L.; Jiao, Y.J.; Yu, C.X.; Zhao, F.; Zhou, X.W.; Liu, Z. Pt, Ag and Au Nanoparticles on Hollow Carbon Spheres as Cathode ORR. *Electron. Mater. Lett.* **2023**, *2023*, 1–8. [CrossRef]
10. Subhan, F.; Aslam, S.; Yan, Z.F.; Yaseen, M.; Naeem, M.; Khan, A. Confinement of Au, Pd and Pt Nanoparticle with Reduced Sizes: Significant Improvement of Dispersion Degree and Catalytic Activity. *Microporous Mesoporous Mater.* **2022**, *337*, 111927. [CrossRef]
11. Meng, G.H.; Zhang, X.Y.; Liu, C.; Wu, J.N.; Guo, X.H.; Liu, Z.Y. Ag Quantum Dot/Montmorillonite Composites with Fluorescent Properties: An Efficient Catalyst. *Res. Chem. Intermed.* **2017**, *43*, 7137–7145. [CrossRef]
12. Nazarian-Samani, M.; Lim, H.D.; Haghighat-Shishavan, S.; Kim, H.K.; Ko, Y.M.; Kim, M.S.; Lee, S.W.; Kashani-Bozorg, S.F.; Abbasi, M.; Guim, H.U.; et al. A Robust Design of Ru Quantum Dot/N-Doped Holey Graphene for Efficient Li-O_2 Batteries. *J. Mater. Chem. A* **2017**, *5*, 619–631. [CrossRef]
13. Kou, J.H.; Varma, R.S. Beet Juice Utilization: Expeditious Green Synthesis of Noble Metal Nanoparticles (Ag, Au, Pt, and Pd) Using Microwaves. *RSC Adv.* **2012**, *2*, 10283–10290. [CrossRef]
14. Xiong, Y.J.; Chen, J.Y.; Wiley, B.; Xia, Y.N.; Aloni, S.; Yin, Y.D. Understanding the Role of Oxidative Etching in the Polyol Synthesis of Pd Nanoparticles with Uniform Shape and Size. *J. Am. Chem. Soc.* **2005**, *127*, 7332–7333. [CrossRef] [PubMed]
15. Jin, M.S.; Zhang, H.; Xie, Z.X.; Xia, Y.N. Palladium Concave Nanocubes with High-Index Facets and Their Enhanced Catalytic Properties. *Angew. Chem. Int. Ed.* **2011**, *50*, 7850–7854. [CrossRef] [PubMed]
16. Xia, Y.N.; Yang, P.D.; Sun, Y.G.; Wu, Y.Y.; Mayers, B.; Gates, B.; Yin, Y.D.; Kim, F.; Yan, Y.Q. One-Dimensional Nanostructures: Synthesis, Characterization, and Applications. *Adv. Mater.* **2003**, *15*, 353–389. [CrossRef]
17. Huo, D.; Kim, M.J.; Lyu, Z.H.; Shi, Y.F.; Wiley, B.J.; Xia, Y.N. One-Dimensional Metal Nanostructures: From Colloidal Syntheses to Applications. *Chem. Rev.* **2019**, *119*, 8972–9073. [CrossRef]
18. Sun, H.Y.; Guo, X.; Ye, W.; Kou, S.F.; Yang, J. Charge Transfer Accelerates Galvanic Replacement for PtAgAu Nanotubes with Enhanced Catalytic Activity. *Nano Res.* **2016**, *9*, 1173–1181. [CrossRef]

19. Zhang, J.W.; Ye, J.Y.; Fan, Q.Y.; Jiang, Y.T.; Zhu, Y.F.; Li, H.Q.; Cao, Z.M.; Kuang, Q.; Cheng, J.; Zheng, J.; et al. Cyclic Penta-Twinned Rhodium Nanobranches as Superior Catalysts for Ethanol Electro-Oxidation. *J. Am. Chem. Soc.* **2018**, *140*, 11232–11240. [CrossRef]
20. Xu, D.D.; Liu, X.L.; Han, M.; Bao, J.C. Facile Synthesis of Ultrathin Single-Crystalline Palladium Nanowires with Enhanced Electrocatalytic Activities. *Chem. Commun.* **2016**, *52*, 12996–12999. [CrossRef]
21. Liu, J.W.; Niu, W.X.; Liu, G.G.; Chen, B.; Huang, J.T.; Cheng, H.F.; Hu, D.Y.; Wang, J.; Liu, Q.; Ge, J.J.; et al. Selective Epitaxial Growth of Rh Nanorods on 2h/Fcc Heterophase Au Nanosheets to Form 1D/2D Rh-Au Heterostructures for Highly Efficient Hydrogen Evolution. *J. Am. Chem. Soc.* **2021**, *143*, 4387–4396. [CrossRef] [PubMed]
22. Kichijo, R.; Miyajima, N.; Ogawa, D.; Sugimori, H.; Wang, K.H.; Imura, Y.; Kawai, T. Water-Phase Synthesis of Au and Au-Ag Nanowires and Their Sers Activity. *RSC Adv.* **2022**, *12*, 28937–28943. [CrossRef] [PubMed]
23. Zhu, X.R.; Hu, Z.; Huang, M.; Zhao, Y.X.; Qu, J.Q.; Hu, S. Au Nanowires with High Aspect Ratio and Atomic Shell of Pt-Ru Alloy for Enhanced Methanol Oxidation Reaction. *Chin. Chem. Lett.* **2021**, *32*, 2033–2037. [CrossRef]
24. Yin, S.L.; Wang, Z.Q.; Qian, X.Q.; Yang, D.D.; Xu, Y.; Li, X.N.; Wang, L.; Wang, H.J. PtM (M = Co, Ni) Mesoporous Nanotubes as Bifunctional Electrocatalysts for Oxygen Reduction and Methanol Oxidation. *ACS Sustain. Chem. Eng.* **2019**, *7*, 7960–7968. [CrossRef]
25. Hong, W.; Wang, J.; Wang, E.K. Rute/M (M=Pt, Pd) Nanoparticle Nanotubes with Enhanced Electrocatalytic Activity. *J. Mater. Chem. A* **2015**, *3*, 13642–13647. [CrossRef]
26. Wang, W.; Chen, X.W.; Zhang, X.; Ye, J.Y.; Xue, F.; Zhen, C.; Liao, X.Y.; Li, H.Q.; Li, P.T.; Liu, M.C.; et al. Quatermetallic Pt-Based Ultrathin Nanowires Intensified by Rh Enable Highly Active and Robust Electrocatalysts for Methanol Oxidation. *Nano Energy* **2020**, *71*, 165705. [CrossRef]
27. Li, M.F.; Zhao, Z.P.; Cheng, T.; Fortunelli, A.; Chen, C.Y.; Yu, R.; Zhang, Q.H.; Gu, L.; Merinov, B.V.; Lin, Z.Y.; et al. Ultrafine Jagged Platinum Nanowires Enable Ultrahigh Mass Activity for the Oxygen Reduction Reaction. *Science* **2016**, *354*, 1414–1419. [CrossRef] [PubMed]
28. Xu, Y.C.; Cui, X.Q.; Wei, S.T.; Zhang, Q.H.; Gu, L.; Meng, F.Q.; Fan, J.C.; Zheng, W.T. Highly Active Zigzag-Like Pt-Zn Alloy Nanowires with High-Index Facets for Alcohol Electrooxidation. *Nano Res.* **2019**, *12*, 1173–1179. [CrossRef]
29. Wang, X.D.; Chen, S.T.; Reggiano, G.; Thota, S.; Wang, Y.C.; Kerns, P.; Suib, S.L.; Zhao, J. Au-Cu-M (M=Pt, Pd, Ag) Nanorods with Enhanced Catalytic Efficiency by Galvanic Replacement Reaction. *Chem. Commun.* **2019**, *55*, 1249–1252. [CrossRef]
30. Yang, H.; He, L.Q.; Wang, Z.H.; Zheng, Y.Y.; Lu, X.H.; Li, G.R.; Fang, P.P.; Chen, J.; Tong, Y. Surface Plasmon Resonance Promoted Photoelectrocatalyst by Visible Light from Au Core Pd Shell Pt Cluster Nanoparticles. *Electrochim. Acta* **2016**, *209*, 591–598. [CrossRef]
31. Guo, S.J.; Wang, L.; Wang, W.; Fang, Y.X.; Wang, E.K. Bifunctional Au@Pt Hybrid Nanorods. *J. Colloid Interface Sci.* **2007**, *315*, 363–368. [CrossRef] [PubMed]
32. Wang, F.; Wang, Z.X.; Shifa, T.A.; Wen, Y.; Wang, F.M.; Zhan, X.Y.; Wang, Q.S.; Xu, K.; Huang, Y.; Yin, L.; et al. Two-Dimensional Non-Layered Materials: Synthesis, Properties and Applications. *Adv. Funct. Mater.* **2017**, *27*, 254. [CrossRef]
33. Liz-Marzán, L.M.; Grzelczak, M. Growing Anisotropic Crystals at the Nanoscale. *Science* **2017**, *356*, 1120–1121. [CrossRef] [PubMed]
34. Hu, H.Q.; Zhou, J.Y.; Kong, Q.S.; Li, C.X. Two-Dimensional Au Nanocrystals: Shape/Size Controlling Synthesis, Morphologies, and Applications. *Part. Part. Syst. Charact.* **2015**, *32*, 796–808. [CrossRef]
35. Huang, H.Z.; Liu, D.; Chen, L.W.; Zhu, Z.J.J.; Li, J.N.; Yu, Z.L.; Su, X.; Jing, X.T.; Wu, S.Q.; Tian, W.J.; et al. Ultrathin Dendritic Pd-Ag Nanoplates for Efficient and Durable Electrocatalytic Reduction of CO_2 to Formate. *Chem. Asian J.* **2023**, *18*, 110. [CrossRef] [PubMed]
36. Liu, H.P.; Zhong, P.; Liu, K.; Han, L.; Zheng, H.Q.; Yin, Y.D.; Gao, C.B. Synthesis of Ultrathin Platinum Nanoplates for Enhanced Oxygen Reduction Activity. *Chem. Sci.* **2018**, *9*, 398–404. [CrossRef] [PubMed]
37. Huang, X.Q.; Tang, S.H.; Mu, X.L.; Dai, Y.; Chen, G.X.; Zhou, Z.Y.; Ruan, F.X.; Yang, Z.L.; Zheng, N.F. Freestanding Palladium Nanosheets with Plasmonic and Catalytic Properties. *Nat. Nanotechnol.* **2011**, *6*, 28–32. [CrossRef] [PubMed]
38. Yang, N.L.; Zhang, Z.C.; Chen, B.; Huang, Y.; Chen, J.Z.; Lai, Z.C.; Chen, Y.; Sindoro, M.; Wang, A.L.; Cheng, H.F.; et al. Synthesis of Ultrathin PdCu Alloy Nanosheets Used as a Highly Efficient Electrocatalyst for Formic Acid Oxidation. *Adv. Mater.* **2017**, *29*, 769. [CrossRef]
39. Hu, P.F.; Yang, H.S.; Chen, S.L.; Xue, Y.F.; Zhu, Q.A.; Tang, M.Y.; Wang, H.; Liu, L.M.; Gao, P.; Duan, X.F.; et al. Hybrid Lamellar Superlattices with Monoatomic Platinum Layers and Programmable Organic Ligands. *J. Am. Chem. Soc.* **2023**, *145*, 717–724. [CrossRef]
40. Sadikin, S.N.; Umar, M.I.A.; Hamzah, A.A.; Nurdin, M.; Umar, A.A. Formation of Ultimate Thin 2D Crystal of Pt in the Presence of Hexamethylenetetramine. *Int. J. Mol. Sci.* **2022**, *23*, 10239. [CrossRef]
41. Yan, S.L.; Chen, C.Z.; Zhang, F.H.; Mahyoub, S.A.; Cheng, Z.M. High-Density Ag Nanosheets for Selective Electrochemical CO_2 Reduction to CO. *Nanotechnology* **2021**, *32*, 165705. [CrossRef] [PubMed]
42. Yan, S.L.; Mahyoub, S.A.; Zhong, J.H.; Chen, C.Z.; Zhang, F.H.; Cheng, Z.M. Ultrathin and Dense Ag Nanosheets Synthesis under Suppressed Face (111) Growth and Surface Diffusion. *J. Power Sources* **2021**, *488*, 229484. [CrossRef]
43. Qiu, X.Y.; Zhang, H.Y.; Wu, P.S.; Zhang, F.Q.; Wei, S.H.; Sun, D.M.; Xu, L.; Tang, Y.W. One-Pot Synthesis of Freestanding Porous Palladium Nanosheets as Highly Efficient Electrocatalysts for Formic Acid Oxidation. *Adv. Funct. Mater.* **2017**, *27*, 1603852. [CrossRef]

44. Zhao, Y.; Bai, J.; Wu, X.R.; Chen, P.; Jin, P.J.; Yao, H.C.; Chen, Y. Atomically Ultrathin Rhco Alloy Nanosheet Aggregates for Efficient Water Electrolysis in Broad Ph Range. *J. Mater. Chem. A* **2019**, *7*, 16437–16446. [CrossRef]
45. Jin, C.H.; Fu, R.J.; Ran, L.Q.; Wang, W.H.; Wang, F.X.; Zheng, D.Z.; Feng, Q.; Wang, G.X. Facile Fabrication of Hierarchical Ultrathin Rh-Based Nanosheets for Efficient Hydrogen Evolution. *RSC Adv.* **2023**, *13*, 13985–13990. [CrossRef] [PubMed]
46. Jang, H.J.; Ham, S.; Acapulco, J.A.I.; Song, Y.; Hong, S.; Shuford, K.L.; Park, S. Fabrication of 2D Au Nanorings with Pt Framework. *J. Am. Chem. Soc.* **2014**, *136*, 17674–17680. [CrossRef]
47. Sang, J.L.; Yu, L.; Song, X.W.; Geng, W.C.; Zhang, Y.; Li, Y.J. Nanoarchitectonics of 2D-Thin and Porous Ag-Au Nanostructures with Controllable Alloying Degrees toward Electrocatalytic CO_2 Reduction. *J. Alloys Compd.* **2023**, *944*, 169155. [CrossRef]
48. Chen, M.; Tang, S.H.; Guo, Z.D.; Wang, X.Y.; Mo, S.G.; Huang, X.Q.; Liu, G.; Zheng, N.F. Core-Shell Pd@Au Nanoplates as Theranostic Agents for in-Vivo Photoacoustic Imaging, CT Imaging, and Photothermal Therapy. *Adv. Mater.* **2014**, *26*, 8210–8216. [CrossRef]
49. Feng, Y.; Liu, H.; Wang, P.F.; Ye, F.; Tan, Q.Q.; Yang, J. Enhancing the Electrocatalytic Property of Hollow Structured Platinum Nanoparticles for Methanol Oxidation through a Hybrid Construction. *Sci. Rep.* **2014**, *4*, 6204. [CrossRef]
50. Chen, Y.; Jiang, X.; Li, Y.; Li, P.; Liu, Q.; Fu, G.; Xu, L.; Sun, D.; Tang, Y. General Strategy for Synthesis of Pd_3M (M = Co and Ni) Nanoassemblies as High-Performance Catalysts for Electrochemical Oxygen Reduction. *Adv. Mater. Interfaces* **2018**, *5*, 1701015. [CrossRef]
51. Qiu, P.T.; Bi, J.L.; Zhang, X.J.; Yang, S.C. Organics- and Surfactant-Free Molten Salt Medium Controlled Synthesis of Pt-M (M = Cu and Pd) Bi- and Trimetallic Nanocubes and Nanosheets. *ACS Sustain. Chem. Eng.* **2017**, *5*, 4205–4213. [CrossRef]
52. Yoo, S.; Cho, S.; Kim, D.; Ih, S.; Lee, S.; Zhang, L.Q.; Li, H.; Lee, J.Y.; Liu, L.C.; Park, S. 3D PtAu Nanoframe Superstructure as a High-Performance Carbon-Free Electrocatalyst. *Nanoscale* **2019**, *11*, 2840–2847. [CrossRef] [PubMed]
53. Hu, S.Z.; Scudiero, L.; Ha, S. Effect of Au and Ru in Au@Pd and Ru@Pd Core@Shell Nanoparticles for Direct Formic Acid Fuel Cells. *ECS Trans.* **2014**, *64*, 1121–1127. [CrossRef]
54. Song, C.Y.; Sun, Y.Z.; Li, J.X.; Dong, C.; Zhang, J.J.; Jiang, X.Y.; Wang, L.H. Silver-Mediated Temperature-Controlled Selective Deposition of Pt on Hexoctahedral Au Nanoparticles and the High Performance of Au@AgPt NPs in Catalysis and Sers. *Nanoscale* **2019**, *11*, 18881–18893. [CrossRef] [PubMed]
55. Gao, F.; Zhang, Y.P.; Ren, F.F.; Shiraishi, Y.; Du, Y.K. Universal Surfactant-Free Strategy for Self-Standing 3D Tremella-Like Pd-M (M = Ag, Pb, and Au) Nanosheets for Superior Alcohols Electrocatalysis. *Adv. Funct. Mater.* **2020**, *30*, 2000255. [CrossRef]
56. Nahar, L.; Farghaly, A.A.; Esteves, R.J.A.; Arachchige, I.U. Shape Controlled Synthesis of Au/Ag/Pd Nanoalloys and Their Oxidation-Induced Self-Assembly into Electrocatalytically Active Aerogel Monoliths. *Chem. Mater.* **2017**, *29*, 7704–7715. [CrossRef]
57. Pan, C.X.; Zheng, Y.Y.; Yang, J.; Lou, D.Y.; Li, J.; Sun, Y.J.; Liu, W. Pt-Pd Bimetallic Aerogel as High-Performance Electrocatalyst for Nonenzymatic Detection of Hydrogen Peroxide. *Catalysts* **2022**, *12*, 528. [CrossRef]
58. Farsadrooh, M.; Saravani, H.; Mehdizadeh, K.; Elyasi, Z.; Javadian, H.; Douk, A.S. Growing Nanoparticles to Assemble a Modern Three-Dimensional Nanoarchitecture of Pt-Ru Aerogel for Advanced Electrocatalysis. *J. Mol. Liq.* **2023**, *384*, 122047. [CrossRef]
59. Oh, A.; Sa, Y.J.; Hwang, H.; Baik, H.; Kim, J.; Kim, B.; Joo, S.H.; Lee, K. Rational Design of Pt-Ni-Co Ternary Alloy Nanoframe Crystals as Highly Efficient Catalysts toward the Alkaline Hydrogen Evolution Reaction. *Nanoscale* **2016**, *8*, 16379–16386. [CrossRef]
60. Chen, G.Z.; Wang, R.Y.; Zhao, W.; Kang, B.T.; Gao, D.W.; Li, C.C.; Lee, J.Y. Effect of Ru Crystal Phase on the Catalytic Activity of Hydrolytic Dehydrogenation of Ammonia Borane. *J. Power. Sources* **2018**, *396*, 148–154. [CrossRef]
61. Tanabe, I.; Ryoki, T.; Ozaki, Y. The Effects of Au Nanoparticle Size (5–60 Nm) and Shape (Sphere, Rod, Cube) over Electronic States and Photocatalytic Activities of TiO_2 Studied by Far- and Deep-Ultraviolet Spectroscopy. *RSC Adv.* **2015**, *5*, 13648–13652. [CrossRef]
62. Si, F.Z.; Chen, X.M.; Liang, L.; Li, C.Y.; Liao, J.H.; Liu, C.P.; Zhang, X.B.; Xing, W. Pt/C Anodic Catalysts with Controlled Morphology for Direct Dimethyl Ether Fuel Cell: The Role of Consecutive Surface. *Electrochim. Acta* **2011**, *56*, 5966–5971. [CrossRef]
63. Zhou, T.; Liu, T.T.; Zhang, Z.Q.; Zhang, G.D.; Wang, F.; Wang, X.F.; Liu, S.Z.; Zhang, H.Z.; Wang, S.S.; Ma, J. Investigation on Catalytic Properties of Au Nanorods with Different Aspect Ratios by Kinetic and Thermodynamic Analysis. *J. Solid State Chem.* **2018**, *263*, 11–17. [CrossRef]
64. Khalil, L.; Sabahat, S.; Ahmed, W. Effect of Aspect Ratio on the Catalytic Activities of Gold Nanorods. *Catal. Lett.* **2023**, *2023*, 1–8. [CrossRef]
65. Sun, S.G.; Xu, H.Y.; Tang, S.H.; Guo, J.S.; Li, H.Q.; Cao, L.; Zhou, B.; Xin, Q.; Sun, G.Q. Synthesis of PtRu Nanowires and Their Catalytic Activity in the Anode of Direct Methanol Fuel Cells. *Chin. J. Catal.* **2006**, *27*, 932–936. [CrossRef]
66. Yang, H.; Wang, Z.H.; Zheng, Y.Y.; He, L.Q.; Zhan, C.; Lu, X.H.; Tian, Z.Q.; Fang, P.P.; Tong, Y.X. Tunable Wavelength Enhanced Photoelectrochemical Cells from Surface Plasmon Resonance. *J. Am. Chem. Soc.* **2016**, *138*, 16204–16207. [CrossRef]
67. Zhang, Q.F.; Zhou, Y.D.; Villarreal, E.; Lin, Y.; Zou, S.L.; Wang, H. Faceted Gold Nanorods: Nanocuboids, Convex Nanocuboids, and Concave Nanocuboids. *Nano Lett.* **2015**, *15*, 4161–4169. [CrossRef]
68. Yue, G.C.; Li, S.; Li, D.M.; Liu, J.; Wang, Y.Q.; Zhao, Y.C.; Wang, N.; Cui, Z.M.; Zhao, Y. Coral-Like Au/TiO_2 Hollow Nanofibers with through-Holes as a High-Efficient Catalyst through Mass Transfer Enhancement. *Langmuir* **2019**, *35*, 4843–4848. [CrossRef]
69. Sadeghi, B.; Meskinfam, M. A Direct Comparison of Nanosilver Particles and Nanosilver Plates for the Oxidation of Ascorbic Acid. *Spectrochim. Acta A* **2012**, *97*, 326–328. [CrossRef]

70. Bukhtiyarov, A.V.; Burueva, D.B.; Prosvirin, I.P.; Klyushin, A.Y.; Panafidin, M.A.; Kovtunov, K.V.; Bukhtiyarov, V.I.; Koptyug, I.V. Bimetallic Pd-Au/Highly Oriented Pyrolytic Graphite Catalysts: From Composition to Pairwise Parahydrogen Addition Selectivity. *J. Phys. Chem. C* **2018**, *122*, 18588–18595. [CrossRef]
71. Elbert, K.; Hu, J.; Ma, Z.; Zhang, Y.; Chen, G.Y.; An, W.; Liu, P.; Isaacs, H.S.; Adzic, R.R.; Wang, J.X. Elucidating Hydrogen Oxidation/Evolution Kinetics in Base and Acid by Enhanced Activities at the Optimized Pt Shell Thickness on the Ru Core. *ACS Catal.* **2015**, *5*, 6764–6772. [CrossRef]
72. Bellini, M.; Pagliaro, M.V.; Lenarda, A.; Fornasiero, P.; Marelli, M.; Evangelisti, C.; Innocenti, M.; Jia, Q.Y.; Mukerjee, S.; Jankovic, J.; et al. Palladium-Ceria Catalysts with Enhanced Alkaline Hydrogen Oxidation Activity for Anion Exchange Membrane Fuel Cells. *ACS Appl. Energy Mater.* **2019**, *2*, 4999–5008. [CrossRef]
73. Mao, J.J.; He, C.T.; Pei, J.J.; Liu, Y.; Li, J.; Chen, W.X.; He, D.S.; Wang, D.S.; Li, Y.D. Isolated Ni Atoms Dispersed on Ru Nanosheets: High-Performance Electrocatalysts toward Hydrogen Oxidation Reaction. *Nano Lett.* **2020**, *20*, 3442–3448. [CrossRef] [PubMed]
74. Alia, S.M.; Pivovar, B.S.; Yan, Y.S. Platinum-Coated Copper Nanowires with High Activity for Hydrogen Oxidation Reaction in Base. *J. Am. Chem. Soc.* **2013**, *135*, 13473–13478. [CrossRef] [PubMed]
75. Dhanya, A.R.; Ganguly, D.; Sundara, R. High temperature annealed (002) oriented WO_3 nanoplatelets with uniform Pt decoration as durable carbon free anode electrocatalyst for PEMFC application. *Int. J. Hydrogen Energy* **2022**, *47*, 24978–24990.
76. Li, H.; Wang, X.; Gong, X.; Liu, C.; Ge, J.J.; Song, P.; Xu, W.L. "One Stone Three Birds" of a Synergetic Effect between Pt Single Atoms and Clusters Makes an Ideal Anode Catalyst for Fuel Cells. *J. Mater. Chem. A* **2023**, *11*, 14826–14832. [CrossRef]
77. Norskov, J.K.; Bligaard, T.; Logadottir, A.; Kitchin, J.R.; Chen, J.G.; Pandelov, S.; Norskov, J.K. Trends in the Exchange Current for Hydrogen Evolution. *J. Electrochem. Soc.* **2005**, *152*, J23–J26. [CrossRef]
78. Mahmood, N.; Yao, Y.D.; Zhang, J.W.; Pan, L.; Zhang, X.W.; Zou, J.J. Electrocatalysts for Hydrogen Evolution in Alkaline Electrolytes: Mechanisms, Challenges, and Prospective Solutions. *Adv. Sci.* **2018**, *5*, 464. [CrossRef]
79. Li, C.J.; Xu, Y.; Yang, D.D.; Qian, X.Q.; Chai, X.J.; Wang, Z.Q.; Li, X.N.; Wang, L.; Wang, H.J. Boosting Electrocatalytic Activities of Pt-Based Mesoporous Nanoparticles for Overall Water Splitting by a Facile Ni, P Co-Incorporation Strategy. *ACS Sustain. Chem. Eng.* **2019**, *7*, 9709–9716. [CrossRef]
80. Zhang, N.; Shao, Q.; Pi, Y.C.; Guo, J.; Huang, X.Q. Solvent-Mediated Shape Tuning of Well-Defined Rhodium Nanocrystals for Efficient Electrochemical Water Splitting. *Chem. Mater.* **2017**, *29*, 5009–5015. [CrossRef]
81. Wang, Q.; Ming, M.; Niu, S.; Zhang, Y.; Fan, G.Y.; Hu, J.S. Scalable Solid-State Synthesis of Highly Dispersed Uncapped Metal (Rh, Ru, Ir) Nanoparticles for Efficient Hydrogen Evolution. *Adv. Energy Mater.* **2018**, *8*, 698. [CrossRef]
82. Li, J.; Li, H.; Zhan, G.M.; Zhang, L.Z. Solar Water Splitting and Nitrogen Fixation with Layered Bismuth Oxyhalides. *Acc. Chem. Res.* **2017**, *50*, 112–121. [CrossRef] [PubMed]
83. Li, Z.; Kong, C.; Lu, G.X. Visible Photocatalytic Water Splitting and Photocatalytic Two-Electron Oxygen Formation over Cu- and Fe-Doped g-C_3N_4. *J. Phys. Chem. C* **2016**, *120*, 56–63. [CrossRef]
84. Liu, C.Y.; Huang, H.W.; Du, X.; Zhang, T.R.; Tian, N.; Guo, Y.X.; Zhang, Y.H. In Situ CO-Crystallization for Fabrication of g-C_3N_4/Bi_5O_7 Heterojunction for Enhanced Visible-Light Photocatalysis. *J. Phys. Chem. C* **2015**, *119*, 17156–17165. [CrossRef]
85. Wang, X.C.; Maeda, K.; Thomas, A.; Takanabe, K.; Xin, G.; Carlsson, J.M.; Domen, K.; Antonietti, M. A Metal-Free Polymeric Photocatalyst for Hydrogen Production from Water under Visible Light. *Nat. Mater.* **2009**, *8*, 76–80. [CrossRef]
86. Zhang, G.G.; Lan, Z.A.; Lin, L.H.; Lin, S.; Wang, X.C. Overall Water Splitting by Pt/G-C_3N_4 Photocatalysts without Using Sacrificial Agents. *Chem. Sci.* **2016**, *7*, 3062–3066. [CrossRef]
87. Claus, P.; Kraak, P.; Schodel, R. Selective Hydrogenation of α,β-Unsaturated Aldehydes to Allylic Alcohols over Supported Monometallic and Bimetallic Ag Catalysts. *Stud. Surf. Sci. Catal.* **1997**, *108*, 281–288.
88. Wei, S.J.; Li, A.; Liu, J.C.; Li, Z.; Chen, W.X.; Gong, Y.; Zhang, Q.H.; Cheong, W.C.; Wang, Y.; Zheng, L.R.; et al. Direct Observation of Noble Metal Nanoparticles Transforming to Thermally Stable Single Atoms. *Nat. Nanotechnol.* **2018**, *13*, 856–861. [CrossRef]
89. Xu, E.Z.; Feng, H.S.; Wang, L.; Zhang, Y.J.; Liu, K.L.; Cui, S.; Meng, H.; Wang, G.R.; Yang, Y.S. Pt Single Atoms and Nanosized Clusters as Catalytic Reaction Platforms for Selective Hydrogenation Applications. *ACS Appl. Nano Mater.* **2023**, *16*, 14991–15001. [CrossRef]
90. Mitsudome, T.; Urayama, T.; Yamazaki, K.; Maehara, Y.; Yamasaki, J.; Gohara, K.; Maeno, Z.; Mizugaki, T.; Jitsukawa, K.; Kaneda, K. Design of Core-Pd/Shell-Ag Nanocomposite Catalyst for Selective Semihydrogenation of Alkynes. *ACS Catal.* **2016**, *6*, 666–670. [CrossRef]
91. Chen, M.; Li, B.L.; Wang, F.; Fang, J.H.; Li, K.; Zhang, C.B. Enhanced CH_4 Selectivity in CO_2 Hydrogenation on Bimetallic Pt-Ni Catalysts with Pt Nanoparticles Modified by Isolated Ni Atoms. *ACS Appl. Nano Mater.* **2023**, *6*, 5826–5834. [CrossRef]
92. Wang, S.H.; Xin, Z.L.; Huang, X.; Yu, W.Z.; Niu, S.; Shao, L.D. Nanosized Pd-Au Bimetallic Phases on Carbon Nanotubes for Selective Phenylacetylene Hydrogenation. *Phys. Chem. Chem. Phys.* **2017**, *19*, 6164–6168. [CrossRef] [PubMed]
93. Matsumoto, S.I. Recent Advances in Automobile Exhaust Catalysts. *Catal. Today* **2004**, *90*, 183–190. [CrossRef]
94. Mahara, Y.; Ohyama, J.; Sawabe, K.; Satsuma, A. Synthesis of Supported Bimetal Catalysts Using Galvanic Deposition Method. *Chem. Rec.* **2018**, *18*, 1306–1313. [CrossRef]
95. Le, P.H.; Yamashita, S.; Cao, K.L.A.; Hirano, T.; Tsunoji, N.; Kautsar, D.B.; Ogi, T. Co Oxidation Enabled by Three-Way Catalysts Comprising Pd/Rh Nanoparticles Supported on Al_2O_3 and $CeZrO_4$ Confined in Macroporous Polystyrene Latex Templates. *ACS Appl. Nano Mater.* **2023**, *6*, 17324–17335. [CrossRef]

96. Li, L.C.; Zhang, N.Q.; Wu, R.; Song, L.Y.; Zhang, G.Z.; He, H. Comparative Study of Moisture-Treated Pd@CeO_2/Al_2O_3 and Pd/CeO_2/Al_2O_3 Catalysts for Automobile Exhaust Emission Reactions: Effect of Core-Shell Interface. *ACS Appl. Mater. Interfaces* **2020**, *12*, 10350–10358. [CrossRef]
97. Yin, X.Y.; Li, S.S.; Deng, J.; Wang, Y.; Li, M.C.; Zhao, Y.; Wang, W.; Wang, J.L.; Chen, Y.Q. Superior Pd-Rh Three-Way Catalyst: Modulating the Surface Composition by Introducing Ceria-Zirconia with Partial K-$Ce_2Zr_2O_8$ Structure as Support. *Ind. Eng. Chem. Res.* **2022**, *61*, 13011–13020. [CrossRef]